Published in final edited form as:
Proc Natl Acad Sci U S A. 2020 December 01; 117(48): 30159–30170. doi:10.1073/pnas.2012025117.

From particle attachment to space-filling coral skeletons

Chang-Yu Sun[a], **Cayla A. Stifler**[a], **Rajesh V. Chopdekar**[b], **Connor A. Schmidt**[a], **Ganesh Parida**[a], **Vanessa Schoeppler**[c], **Benjamin I. Fordyce**[a], **Jack H. Brau**[a], **Tali Mass**[d], **Sylvie Tambutté**[e], **Pupa U.P.A. Gilbert**[a,f,g,h,1,2]

Patricia M. Dove
Virginia Technical Institute, Blacksburg, VA

[a]Department of Physics, University of Wisconsin, Madison, WI 53706

[b]Advanced Light Source, Lawrence Berkeley National Laboratory, Berkeley, CA 94720

[c]B CUBE–Center for Molecular Bioengineering, Technische Universität Dresden, 01307 Dresden, Germany

[d]Marine Biology Department, University of Haifa, 31905 Haifa, Israel

[e]Marine Biology Department, Centre Scientifique de Monaco, 98000 Monaco, Principality of Monaco

[f]Department of Chemistry, University of Wisconsin, Madison, WI 53706

[g]Department of Geoscience, University of Wisconsin, Madison, WI 53706

[h]Department of Materials Science, University of Wisconsin, Madison, WI 53706

Abstract

Reef-building corals and their aragonite ($CaCO_3$) skeletons support entire reef ecosystems, yet their formation mechanism is poorly understood. Here we used synchrotron spectromicroscopy to observe the nanoscale mineralogy of fresh, forming skeletons from six species spanning all reef-forming coral morphologies: Branching, encrusting, massive, and table. In all species, hydrated and anhydrous amorphous calcium carbonate nanoparticles were precursors for skeletal growth, as previously observed in a single species. The amorphous precursors here were observed in tissue, between tissue and skeleton, and at growth fronts of the skeleton, within a low-density nano- or microporous layer varying in thickness from 7 to 20 μm. Brunauer-Emmett-Teller measurements, however, indicated that the mature skeletons at the microscale were space-filling, comparable to single crystals of geologic aragonite. Nanoparticles alone can never fill space completely, thus ion-by-ion filling must be invoked to fill interstitial pores. Such ion-by-ion diffusion and attachment

[2]To whom correspondence may be addressed. pupa@physics.wisc.edu.
[1]Previously publishing as Gelsomina De Stasio.

Author contributions: T.M. and P.U.P.A.G. designed research; C.-Y.S., C. A. Stifler, V.S., T.M., S.T., and P.U.P.A.G. performed research; R.V.C., J.H.B., and P.U.P.A.G. contributed new reagents/analytic tools; C. A. Schmidt, G.P., B.I.F., and P.U.P.A.G. analyzed data; S.T. and P.U.P.A.G. developed the model of Fig. 6; and P.U.P.A.G. wrote the paper with contributions from all authors.

The authors declare no competing interest.

Europe PMC Funders Author Manuscripts

may occur from the supersaturated calcifying fluid known to exist in corals, or from a dense liquid precursor, observed in synthetic systems but never in biogenic ones. Concomitant particle attachment and ion-by-ion filling was previously observed in synthetic calcite rhombohedra, but never in aragonite pseudohexagonal prisms, synthetic or biogenic, as observed here. Models for biomineral growth, isotope incorporation, and coral skeletons' resilience to ocean warming and acidification must take into account the dual formation mechanism, including particle attachment and ion-by-ion space filling.

Keywords

coral skeleton formation; PEEM; spectromicroscopy; biomineral; aragonite

Coral reef ecosystems cover less than 1% of ocean floors, yet they host 25% of all marine species. In recent years these diverse and important ecosystems have sustained significant declines due to ocean warming and acidification (1–5), and require urgent intervention to survive beyond 2050, when coral reef sediments, including the skeletons of dead corals, will transition from net precipitation to net dissolution (6).

Together with coralline algae, bacteria, and other organisms, scleractinian or stony corals deposit a hard skeleton and gradually build up the complex 3D rigid structure of a reef. As the name "coral reef" suggests, compared to other reef-builders, corals are the primary builders of the reef framework structure (7), and the formation of their skeletons is essential to sustain reef ecosystems. Reef-building corals are colonial organisms composed of individual animals, the polyps, which are all genetically identical and connected to one another. In symbiotic corals, which are the majority of reef-building corals, each polyp hosts many endosymbiont dinoflagellate algae from the Symbiodiniaceae family. These algae photosynthesize, supply the polyps with oxygen, glucose, glycerol, and amino acids, and thus provide most of the input the animal needs for its metabolism and the complex skeleton formation mechanisms (8–10).

Like many other biominerals, coral skeletons are composites (11) of 97.5 w% aragonite ($CaCO_3$), 0.07 w% organics (12), and up to 2.5 w% water associated with organics (13). Among the organics, many proteins are involved in skeleton formation (14–16), where they can play both structural and kinetic roles, but the function of only a few proteins is thus far known.

The morphology and crystal structure of coral skeletons and their layer-by-layer deposition are well understood (9, 17–19). The aragonite structures include nanoparticulate centers of calcification (CoCs), rich in Mg and organics (20), elongated acicular crystals termed fibers, radiating out of CoCs, and forming plumose spherulites (21), with their crystalline *c*-axes along the radial direction (21), and randomly oriented crystals called sprinkles, which were only recently observed and were proposed to be proto-fibers: That is, the first nucleated seed of each fiber crystal (22). When sprinkle crystal *c*-axes are radially oriented they elongate radially to become fibers; when they are not, they can't grow and thus remain microscopic (0.2 to 20 μm), or they disappear in a coarsening process (22).

Europe PMC Funders Author Manuscripts

The mechanism of crystal growth, either ion by ion or particle by particle (23), in coral skeleton is poorly understood and a subject of intense investigation (15, 22, 24–28), especially because it is relevant to understand how corals are responding to climate change, including ocean acidification and warming (1–5, 18, 28). Because the crystal deposition and growth mechanisms are not yet understood, they cannot be used to maximize the impact of interventions and decision making (29, 30). Crystal growth in corals has been thought for a long time to be a purely physicochemical process in which crystals grow one ion at a time from a calcifying fluid (CF) (31, 32). Recently, Mass et al. (33) showed evidence that one species of coral, *Stylophora pistillata*, deposits its skeleton by attachment of amorphous calcium carbonate (ACC) particles, as previously observed in many other biominerals (34–39). It is unknown if other reef-building corals also form their skeletons by particle attachment, and if particles are the only source of growth material or if ions also attach to growing crystals. In the present work we address these two unknowns.

The current understanding is that the particles attaching to form skeletons are first formed intracellularly, within membranebound intracellular vesicles. Starting from the CF, located between the biomineralizing cells (calicoblastic cell layer, apical side) and the biomineral growth front, calcium is incorporated into each cell by macropinocytosis, as recently demonstrated by Ganot et al. (see figure 10 in ref. 25). Macropinocytosis produces 350- to 600-nm membrane-bound, intracellular vesicles, which move through the cell cytoplasm and are then exocytosed back into the CF. Such macropinocytosis is ubiquitous in corals and anemones (25). Intracellular vesicles rich in Ca are membrane-bound; that is, they are surrounded by a phospholipid bilayer with proteins that was previously the cell membrane at the apical side. This bilayer surrounds the vesicle, as long as it is intracellular, and then fuses again with the apical membrane when the content of the vesicle is exocytosed and released into the CF. Membrane-bound, intracellular vesicles enriched in calcium and transporting it to the biomineralization site were not only observed in corals and anemones (25), but also in sea urchin embryos (40). Vesicles carrying ACC are extracellular in chicken eggshell formation, but they are also membrane-bound (41).

Mass et al. (33) observed a myriad of 400-nm Ca-rich spots in living *S. pistillata* corals, which could be either solid or liquid. Venn et al. (42) observed pools of CF with elevated pH in living *S. pistillata* corals. They did not observe such spots in the calicoblastic cell layer. Thus, the intracellular vesicles do not contain elevated-pH liquid droplets. Together, these observations suggest that the intracellular vesicles contain solid ACC particles, not liquid solution droplets, although the exact state of hydration and viscosity remain uncertain. Liquid droplets were the expected result from the liquid–liquid phase separation (LLPS) observed in calcium carbonates grown in vitro by the polymer-induced liquid precursor (PILP) process (43), or predicted by molecular dynamics simulations (44).

To investigate how widespread particle attachment is in coral skeleton formation, we analyzed the widest possible variety of species, by selecting at least one representative from each reef-building coral morphology, including branching, massive, encrusting, and table corals (Table 1 and SI Appendix, Table S1). The analysis was done with synchrotron X-ray PhotoEmission Electron Microscopy (PEEM), and component mapping (38) to spatially map and quantify the mineral phases present (33). All of these corals and their forming

skeletons were analyzed when they were freshly killed, and their tissues adjacent to the skeleton were preserved to show intratissue precursor phases and to protect the forming skeleton surface.

To investigate if particle attachment is the only mechanisms, or ion attachment should be considered as well, we measured how space-filling coral skeletons are in various species, using Brunauer-Emmett-Teller (BET), and compared the results with nonbiogenic geologic aragonite.

To compare space-filling of surface versus bulk in coral skeleton cross-sections, we used polarized light microscopy (PLM), which in the forming part of the skeleton is aided by "form birefringence" in the porous surface, which is rich in anisotropic particles (45–47).

Results

We tested the hypothesis that coral skeleton formation occurs by attachment of amorphous particles, and whether or not there is also concomitant ion-by-ion attachment. The analysis included five new reef-building species, and one previously published and repeated here for consistency. All species are listed in Table 1. The eight subheadings below describe experimental observations.

Reef-Building Coral Skeletons Are Nanoparticulate

The fractured surfaces of all five coral skeletons in Fig. 1, observed with high-resolution scanning electron microscopy (SEM), appear nanoparticulate. By comparison, nonbiogenic geologic aragonite (27) or synthetic aragonite grown ion by ion from solution are completely smooth and feature-free at the same magnification as Fig. 1 *A4–E4* (50,000×). See also figure 3 and SI Appendix figure S2 in Gilbert et al. (27). Thus, all skeletons formed by all reef-building corals exhibit nanoparticulate fracture figures, suggesting that they may form by attachment of particles.

The Particles Attaching to Growing Coral Skeletons Are Amorphous

Fig. 2 *A* and *B* show that the tissues surrounding the coral skeleton were well preserved at least at the microscale. At the nanoscale tissues must have been significantly altered with respect to their native state by fixation and dehydration. If any mineral phases are detected within the tissue, however, they may provide the most informative and direct observation of the skeleton deposition process thus far obtained.

We used the same PEEM spectromicroscopy methods in Mass et al. (33), and confirmed that all skeletons indeed share the same amorphous precursor phases, and that these are localized preferentially near the forming surface (Fig. 2 *C* and *D*). Specifically, the precursor phases are hydrated (ACC-H_2O) and anhydrous ACC, displayed in red and green, respectively, in Fig. 2 *C* and *D*. We did not include poorly crystalline aragonite (pAra) as done by Mass et al. (33) and DeVol et al. (39); because after careful analysis all single-pixel spectra were best fitted by three rather than by four components, the fourth pAra component, therefore, was omitted. These and all other component maps in this work were obtained using a new, more conservative set of component spectra, presented in SI Appendix, Fig. S1.

For each of the five new and one repeat species, one sample was prepared, in which 5 to 15 areas were analyzed, each area approximately (60 μm)^2 in size. Fig. 2 *C* and *D* are two examples of such areas. All six species gave consistent results in component mapping, as presented in Fig. 3: They exhibited nanoscale particles of ACC-H_2O and ACC, all of which were observed at or near the forming surface of the skeletons but never in the mature, fully formed skeleton fibers. Amorphous pixels in Fig. 3 *A4–F4* and *A5–G5* appear as nonblue pixels; that is, red, green, and mixed colors cyan, magenta, and yellow. Amorphous nanoparticles persisted in the CoCs (Fig. 3 *A5*) as found previously, even a decade after the death of the animal (33, 39). Isolated nanoparticles were observed in all species either in the tissue or in between the tissue and skeleton surface. They were especially abundant in *Montipora turgescens* and *Turbinaria peltata* (Fig. 3 *D3* and *E3*). They were all solid at the time of the analysis and were found to be either amorphous or crystalline aragonite (Fig. 3 *D4*, *D5*, *E4*, and *E5*). All three phases were also observed in cross-sections of calicoblastic cells in *S. pistillata* (Fig. 3 *G2–G5* and SI Appendix, Fig. S5).

All areas in Fig. 3 were representative of all 5 to 15 areas analyzed in each species and were acquired in duplicate with consistent results (see SI Appendix, Table S1 for postmortem acquisition times and file names showing repeated acquisitions).

The particles in the tissue or between tissue and growing skeleton surface showed consistently more amorphous spectra than skeletons, as visualized by pixel colors. Pixels containing amorphous precursor phases (nonblue colors) were observed in the tissue (Fig. 3 *A4*, *C5*, *E4*, *E5*, *G4*, and *G5*) or between tissue and skeleton (Fig. 3 *B4* and *B5*) or on the surface of the forming skeletons (Fig. 3 *C5*, *F4*, and *F5*) with higher frequency than in the bulk of the skeletons, which were mostly aragonite (blue) (panels 3 in Fig. 3 *A–G*).

The Forming Surface of Coral Skeletons Is Porous

The same Ca L-edge data used for component mapping can be used to image the calcium concentration [Ca] in spatial distribution maps. These [Ca] maps showed, unexpectedly, that the density of Ca in a 7- to 8-μm-thick layer at the coral skeleton growth front was lower than in the mature skeleton, a difference most pronounced in *Micromussa lordhowensis* (Fig. 4*A*) but consistently observed in most species.

Although ACC-H_2O has lower density than crystalline aragonite, this phase is not the cause of the low-[Ca] 7- to 8-μm band. Component mapping of PEEM spectra from the low-[Ca] band showed crystalline aragonite in the vast majority of pixels (Fig. 4*B*). A possible interpretation is that the band was composed of nanoporous aragonite with pore sizes smaller than the 60-nm pixel resolution of PEEM images.

In *Acropora* sp., instead of a low-[Ca] band, an evident microporous aggregate was observed at the surface (~15-μm-thick) (Fig. 4 *D*). In both cases, nano- and microporous aggregates were confined to the growth front. The bulk skeleton (>15 μm from the surface) appeared to be space-filling in all [Ca], component, and polarization-dependent imaging contrast (PIC) maps (right side of each image in Fig. 4).

The nano- and micropores at the surface of all coral skeletons were infiltrated with the embedding epoxy resin and were thus polished to a flat surface for PEEM analysis.

The unexpected observation of surface porosity in *Micromussa* and *Acropora* raises two questions: Whether or not the surfaces of other corals are porous, and whether or not such surface porosity can be observed with other methods, more widely available than PEEM. To answer these questions, we analyzed the surfaces of all coral skeletons with SEM and observed that indeed they are all porous. In most cases the native, non-fractured surface of coral skeleton enveloped by the polyp in the living coral exhibits either aragonite acicular (needle-like) crystal fibers or nanoparticles with irregular shape. These are shown in Fig. 5, at increasing magnifications for the five new species. Fibers are visible at native surfaces in Fig. 5 *A3*, *B3*, *C3*, and *E3* and nanoparticles in Fig. 5 *D3*. Some surfaces show pores within fibers, such as those indicated by arrows in Fig. 5 *B3*, *C3*, and *E3*.

We also addressed the surface porosity questions with PLM images of polished coral skeletons, which demonstrate nanoscale porosity of the skeleton growth fronts. PLM images appear bright and with a myriad of colors due to form birefringence. Fig. 2 *A* shows a region of *T. peltata* in which a bright colorful band is evident all along the growth front. A brighter and colorful growth front is observed in *S. pistillata* as well (SI Appendix, Fig. S2).

In conclusion, once discovered using a sophisticated synchrotron method, the micro- or nanoporous growth front can be recognized using more conventional methods. Of course, this nano- and microporosity has nothing to do with the millimeter-scale surface porosity, termed skeletal cups or corallites, common to all corals, which are the holes where each polyp lives and retracts its tentacles when threatened or handled.

Mature Coral Skeletons Are Space-Filling

We analyzed coral skeletons using BET measurements of the specific surface area, to determine whether or not the bulk, mature skeleton was space-filling at the nanoscale. Typical readings in BET indicate that nanoporous materials such as aggregated nanoparticles have large surface areas, on the order of hundreds of square meters per gram of powder (~100 to 300 m^2/g), whereas space-filling macroscopic single crystals, such as geologic calcite or aragonite, have significantly smaller surface areas (~1 to 5 m^2/g) (48). In the BET measurements here, all coral skeletons showed surface areas smaller than 4 m^2/g, thus they filled space as much as single crystals of nonbiogenic geologic aragonite, as shown in Table 2.

Despite the inferred nano or evident microporosity of the growing surfaces, the bulk of the skeletons were dense and space-filling in all corals, unlike aggregates of nanoparticles that exhibited 100 to 300 m^2/g areas (49), as also indicated in Table 2. Thus, mature coral skeletons are space-filling.

Ion-by-Ion Filling of Interstitial Pores May Explain Space-Filling

The present data do not reveal the rate at which the amorphous nanoparticles were formed or deposited on the growing crystallized aragonite skeleton. They also cannot determine whether the crystallization occurred as a solid-state transformation, via dehydration and

crystallization steps, or via dissolution–reprecipitation. Given the unavoidable sample preparation time between the death of the animal and the analysis, which was 22 h for the *M. lordhowensis* and 16 h for *Acropora* sp. in Fig. 4, crystallization could have occurred either rapidly in vivo or as a consequence of or spontaneously during sample preparation. Given that the typical coral linear growth rate is 15 to 40 μm/d, which is quite fast, even in slow-growing corals (33, 50, 51), and because recent in vivo confocal Raman spectroscopy data did not report ACC at the forming surface (20, 52), the transformation is likely prompt.

The observation that a higher-density, space-filling, mature bulk skeleton develops from a lower-density porous surface region of freshly deposited biomineral necessitates a role for ion-by-ion growth. Liquid-phase transport and ion attachment is the only known process to reduce porosity, whereas particle transport or reorganization cannot, alone, reduce porosity (53). Although the excess free energy of high surface area porous materials could provide a thermodynamic driving force for porosity reduction by ions, this is very slow at biologically relevant temperatures. A high liquid-phase concentration of Ca and CO_3^{2-}, as expressed by the saturation state of the solution with respect to aragonite, Ω_{arag}, would provide a driving force both for diffusive transport into the porous biomineral and for ion attachment, leading to aragonite growth, gradual porosity loss, and eventually space-filling. Such high-supersaturation solution has indeed been previously observed in living corals as they form skeletons, is termed CF (42), and its chemical composition was recently measured in vivo (26). Based on those measurements, Ω_{arag} can be calculated using the formula:

$$\Omega_{\text{arag}} = \frac{\left[\text{Ca}^{2+}\right]\left[\text{CO}_3^{2-}\right]}{K_{sp}},$$

where the solubility product is $K_{sp} = 7.184$, as obtained by Sevilgen et al. (26) using the salinity values in Mucci (54). Using this formula, Sevilgen et al. (26) found that Ω_{arag} is 12 in CF, far greater than the current seawater $\Omega_{arag} = 3$, and the thermodynamic requirement for ion-by-ion growth $\Omega_{arag} > 1$.

Furthermore, it is possible that nanodroplets of a dense liquid precursor phase fill the interstitial space between the nanoparticles deposited at the surface. Such dense liquid precursors, termed PILP, have been observed extensively in synthetic calcium carbonate systems (43, 55, 56), but thus far never in biogenic ones.

Whether the filling of interstitial pores occurs from a supersaturated CF, PILP droplets, or from both, the process of filling must occur ion by ion, because solid nanoparticles of any size could never fill space as completely as coral skeletons do (Table 2). Thus, we term this observation “ion-by-ion filling” in corals skeletons.

A Closed-System Model for Coral Skeleton Formation, with a Dual Mechanism: Crystallization by Attachment of Particles and Ions

The two co-occurring formation mechanisms, particle attachment and ion-by-ion filling, are described in the model in Fig. 6. This model is a substantial advance in our understanding of

how corals form their skeletons. It is distinct from the previous model by Mass et al. (33) in important conceptual aspects.

First, the calicoblastic tissue (forming the skeleton) is not in direct contact with the growing biomineral, as proposed by Mass et al. (33). The present model includes the CF (yellow in Fig. 6), which has now been fully documented and analyzed (24, 26, 32, 42, 57). By means of membrane transporters, the CF is enriched with respect to seawater in [Ca] (13 vs. 11 mM), in carbonate ion concentration (700 vs. 200 μM/kg), in supersaturation with respect to aragonite (Ω_{arag}~12 vs. 3) (26), and in pH (8.5 vs. 8) (26). All of these factors make it possible not only to prevent dissolution of the ACC-H_2O or ACC nanoparticles formed in vesicles within the calicoblastic cells (red in Fig. 6) and deposited on the forming skeleton, but also to induce ion-by-ion filling in interstitial spaces.

Second, the present model includes a porous surface in which solid particles have already attached, but ions from liquid droplets or CF have not yet attached. Ion-by-ion filling of nanoparticle interstitial space is necessary based on the data presented here. Specifically, the space-filling nature of coral skeletons reported here (Table 2) is incompatible with particle attachment alone, thus a new mechanism must be introduced.

Third, the ACC particles formed intracellularly do not, as in Mass et al. (33), originate from seawater or from other tissues on the outer side, but on the apical side of the calicoblastic cells, as shown by Ganot et al. (25). This is shown by the yellow-to-red vesicles and arrow Fig. 6. The CF is taken up into a calicoblastic cell by macropinocytosis (25). The intravesicle fluid is actively and biologically enriched in Ca, HCO_3^-, other ions, and organics; protons are removed so that solid ACC-H_2O nanoparticles can form intracellularly (red in Fig. 6). The intracellular, partly amorphous Ca-rich clusters observed within calicoblastic cells in Fig. 3 *G5* and SI Appendix, Fig. S5 support the idea that ACC-H_2O nanoparticles are already solid when they are still in cells.

Fourth, organic secretions into the CF and the vesicles can, and most likely do, have other effects as well.

Fifth, once formed, the ACC-H_2O nanoparticles are exocytosed into the CF and attach to the growing skeleton surface. Gradually the solid aggregate of nanoparticles and ions dehydrates (green in Fig. 6), crystallizes (blue in Fig. 6), and ion attachment fills interstitial spaces.

Sixth, crystalline fibers radiate from CoCs and form spherulites (21, 22), as each crystal fiber grows at the expense of the amorphous precursor phases. All three mineral phases persist in CoCs, as previously observed (33, 39).

Seventh, Ostwald ripening, coarsening by dissolution and reprecipitation, or a dense liquid precursor phase in the CF are all included in this model.

Direct Evidence of Concomitant Particle Attachment and Ion Filling

We searched for direct evidence in all skeletons with diverse methods to find at least one convincing example of the dual mechanism proposed here and summarized in the model of Fig. 6. We found two adjacent areas on the native surface of *T. peltata*, in which forming

coral skeleton fibers exhibit clear, euhedral, crystal-line, space-filling parts as well as nanoparticulate, porous parts, as shown in Fig. 7. We stress that the images in Fig. 7 were acquired on the native surface, in contact with the polyp in the original living coral and not on a fractured surface. One cannot, therefore, know which parts were formed first in these images. The colored image in SI Appendix, Fig. S3 shows interspersed space-filling euhedral and nonspace-filling nanoparticulate parts, colored in blue and green, respectively, and these are interspersed in each forming fiber, suggesting that they may have formed simultaneously.

Amorphous nanoparticles are more soluble than euhedral aragonite crystals (58). If dissolution and reprecipitation during sample preparation and handling had occurred, amorphous nanoparticles should have dissolved preferentially and disappeared, but they are still observed in Fig. 7 and SI Appendix, Fig. S3, again suggesting that crystallization is prompt. Furthermore, any artifact reprecipitation, not under biological control, would be expected to occur on any surface, not preferentially in some locations and not others, as observed in Fig. 7 and SI Appendix, Fig. S3. Therefore, we tentatively conclude that these fibers appeared postmortem at the SEM similar to how they appeared in the living animal.

Euhedral Amorphous Particle Attachment

A striking observation in Fig. 7*A* is the appearance of nanoparticles aligned along lines parallel to the outer perimeter of the euhedral pseudohexagonal prisms, highlighted by arrows in Fig. 7*A* . A possible interpretation is that amorphous nanoparticles attach to flat surfaces and migrate preferentially to kinks or steps of growing crystals, just like single ions do in classic ion-by-ion growth from solution, thus leading to euhedral crystal habit. This phenomenon was previously observed and interpreted by Gal et al. (59) for synthetic ACC nanoparticles attaching to form a rhombohedron of calcite. [See figure 2 in Gal et al. (59) for the experimental result, and figure 7 in Gal et al. (59) for the explanation of the phenomenon.] To our knowledge, such euhedral attachment of amorphous particles has not previously been observed in either synthetic or biogenic aragonite crystals.

Discussion

The previous observation by Mass et al. (33) that *S. pistillata* forms its skeleton by attachment of amorphous particles was confirmed here by repeat experiments on the same species and five additional reef-building corals: *Acropora* sp., *Blastomussa merleti*, *M. lordhowensis*, *M. turgescens*, and *T. peltata*.

In support of particle attachment, both the observation of ACC phases near the skeleton growth surfaces (Fig. 3) and the low-density surface band (Fig. 4), are incompatible with ion-by-ion–only growth of crystalline aragonite. This is a robust conclusion, not contradicted by any of the rich and debated ideas about calcium carbonate nucleation and growth. Surface nanoparticles have been observed on fresh coral skeletons (20) and in their cross-sections (27), and shown here in Figs. 1, 5, and 7 and SI Appendix, Fig. S3. Thus, amorphous precursor nanoparticles deposited on the surface of the growing skeleton are a key component of the coral skeleton growth mechanism. The model proposed here, summarized in Fig. 6, includes both ion and particle attachment.

In support of ion-by-ion crystal growth, BET analysis shows that coral skeletons are space-filling (Table 2). Aggregating particles of any size cannot fill space as completely as single crystals of aragonite. Aggregates of nanoparticles are extremely porous (49), thus the interstitial space between nanoparticles in coral skeletons must be filled ion by ion. This dual mechanism of crystal growth, including both ion and particle attachment, is the most relevant result of this work. It is not only deduced as a logical conclusion of the space-filling data, but also observed side-by-side by SEM within the same coral skeleton fibers in Fig. 7 and SI Appendix, Fig. S3.

One possibility is that the ion-by-ion filling occurs from a dense liquid precursor to coral skeleton formation (43, 55, 56), but this possibility has never been demonstrated in any biogenic mineral. Another possibility is that dissolution and reprecipitation occur as the amorphous particles aggregate at the skeleton growth front, and are immersed in the highly supersaturated CF, or a third possibility is that ions from the CF precipitate and fill interstitial spaces. With the current knowledge and data, there is no way to select one of these hypotheses as the most likely. All three hypotheses have in common ion attachment from solution to the growing biomineral, thus they can all be encompassed into the “ion attachment” mechanism. We propose a model that incorporates particle attachment and ion attachment from the CF (Fig. 6). This model is consistent with all of the experimental evidence currently available (22, 25, 26, 33, 42, 60, 61) and supersedes the incomplete model proposed by Mass et al. (33).

Since the intracellular vesicles are membrane-bound, and all biological phospholipid bilayer membranes are closed systems, any transport across vesicle membranes occurs under strict and active biological control, not by simple diffusion. The same transmembrane transporters that greatly enrich the CF must be active in the vesicle membranes as well. In fact, these are the same phospholipid bilayer membranes, including the same transporters that are at times at the apical side of the calicoblastic cells, and at times forming intracellular vesicles.

The intracellular concentration of Ca is low, in the nanomolar range, in calicoblastic cells as in any other eukaryotic cell, which is much lower than the seawater concentration of 10 to 11 mM. Millimolar intracellular Ca is toxic to eukaryotic cells (62). Ca, therefore, must be actively removed from the cytoplasm, and either sequestered in the endoplasmic reticulum or, for biomineralizing organisms, in the biomineral or the biomineral-precursor particles in vesicles, or in the CF.

Holcomb et al. (see figure 1 in ref. 63) showed with in vitro experiments that aragonite crystal growth, not nucleation, can occur and is favored at $\Omega = 12$, whereas above $\Omega = 20$ nucleation occurs. Nucleation and growth of ACC-H_2O must occur at slightly, not significantly, different values of Ω. Thus, at the observed $\Omega = 12$ in the CF ion-by-ion growth occurs, but not nucleation of either ACC or aragonite. Nucleation of solid ACC-H_2O must be initiated under biological control within the intracellular vesicles. How, precisely, this occurs is unclear, especially if transporters and biological controls are identical in both CF and intracellular vesicles. One possibility is that in the confined space of a vesicle Ca^{2+} and CO_3^{2-} ions increase the supersaturation to $\Omega > 20$.

Previous experiments by TambuttÉ et al. (64) showed that calcein-stained seawater only gets to the mineralization site via the paracellular transport route (24, 65), not by vacuolization of seawater, as observed by Erez in foraminifera (66). Ganot et al. (25) showed that macropinocytosis is ubiquitous in corals and anemones, and that it occurs on the apical side of the calicoblastic endothelium, which is the bottom side of the cell layer, in the schematic of Fig. 6. Thus, Ca ions in seawater reach the CF, are endocytosed into intracellular vesicles (25), exocytosed again into the CF (25), and finally are incorporated into the biomineral (64).

The isotopic composition of crystals grown by particle or ion attachment may differ. In vitro experiments to distinguish the isotopic signature of the two distinct formation mechanisms are highly desirable, but they have not been done yet. Trace element composition, however, varies, depending on which of the two mechanism is at play, as shown by Blue et al. (67), thus the isotopic signatures are expected to differ as well. The extent of ion- or particle-attachment contributions to coral skeleton deposition may vary corresponding to the observed isotopic variations under various controls, biological or physical, including photosynthesis (68), seasonality (69), temperature (70), and acidification (71), to which corals may respond by decoupling CF composition from seawater pH (57).

The PLM images presented here demonstrate form birefringence (45) in coral skeletons (Fig. 2 and SI Appendix, Fig. S2). This optical phenomenon can be and indeed was observed in diatom biosilica cell walls or in any other nanolayer or nanogranular material, crystalline or amorphous, organic or mineral, as long as the nanostructures are anisotropic in shape (46, 47). In corals, form birefringence is useful because it demonstrates nanoscale porosity of the skeleton partly formed growth fronts, which in turn demonstrates formation by particle attachment using PLM, which is widely available and commonly termed “crossed polarizers” microscopy.

The response of coral reefs to ocean warming and acidification depends on a variety of processes upstream of calcification (1–5). How corals form their skeletons is key to understanding their response to increasing environmental stressors. The model for coral skeleton formation presented here is a modest first step. With this model, the response of corals to heat and acidification stressors can be tested on a large scale, especially using the simple, widely available methods, PLM and SEM, shown here to be extremely informative about how corals deposit their skeletons.

Materials and Methods

Samples. Twenty living corals were maintained at Albany Aquarium, Albany, CA. The 20 samples were from a variety of species, and most of them were used for practice purposes before beamtime to optimize logistics and sample preparation protocols. Only the top six samples described in Table 1 were actually used for PEEM and DNA analysis, which was done over a period of 4 y. Each of the six samples was analyzed during beamtime and prepared in as short a time as possible between the death of the animal and the analysis. The *S. pistillata* samples in Fig. 3 are from the same batch prepared for Mass et al. (33), and were treated identically to all other species, except for the omission, in that earlier

preparation, of $MgCl_2$, which was used in the five new species to relax the tissue. The two protocols give similar results.

Unfortunately, the process of skeleton deposition cannot be observed in living corals with nanoscale resolution and spectroscopic identification of mineral phases. The animal must be killed (fixed), dehydrated, embedded, and polished to expose a flat surface for nanoscale lateral resolution and probing depth.

The sample preparation used here is aimed at preserving of the tissue attached to the skeleton. This is for two reasons. First, because the natural polyp tissue is the best protector of the forming skeleton surface, especially to retain, to the extent possible, extremely soluble amorphous precursor minerals; second, because it is desirable to observe precursor minerals within the tissue, where they are formed.

Each of the living corals was removed from the aquarium at Albany Aquarium, immersed in seawater to which 5 w% $MgCl_2$ was previously dissolved, and transported at room temperature for 30 min to the Advanced Light Source. We noticed on day 1 that the polyps retract when touched; thus, in order to maintain the most natural tissue position with respect to the skeleton, we used 5 w% $MgCl_2$ solution to relax the tissue. In in vitro experiments $MgCl_2$ inhibits the nucleation of calcite and thus helps the precipitation of ACC. In seawater there is already a high concentration of Mg, and precipitation of calcite or ACC does not occur, either at the natural seawater Mg concentration (54 μM) or at the approximately doubled concentration used here (54 + 53 μM).

At the Advanced Light Source, a small piece of tissue was cut off, immersed in 100% ethanol, and frozen at −20 °C for later DNA analysis.

Solutions prepared were as follows:

- 22 g/L Na_2CO_3 in water filtered 0.2 μm.
- Buffer 1: 0.05 M Na Cacodylate buffer in 22 g/L Na_2CO_3;

  add 10.7 g Na Cacodylate powder to 1000 mL 22 g/L Na_2CO_3 solution.
- Buffer 2: 0.002 M Na Cacodylate buffer in 1 g/L Na_2CO_3;

  add 0.086 g Na Cacodylate powder to 200 mL 1 g/L Na_2CO_3 solution.
- Buffer 3: 0.002 M Na Cacodylate buffer in 0.5 g/L Na_2CO_3;

  add 0.086 g Na Cacodylate powder to 200 mL 0.5 g/L Na_2CO_3 solution.
- Fixative: 2% Formaldehyde in Na Cacodylate buffer;

  add one 10 mL ampule of 16% Formaldehyde to 70 mL of Buffer 1.

The coral sample was immersed in Fixative for 30 min, rinsed twice in Buffer 1, gradually dehydrated in Buffer 2 with 50%, 60%, and 70% ethanol (vol/vol), 50 mL and 10 min for each step. The sample was further dehydrated in Buffer 3 with 80% and 90% ethanol (vol/vol), and then twice in 100% ethanol, 50 mL and 10 min for each step.

The fixed and dehydrated sample was cut into smaller pieces, each ~1 cm^3, still in ethanol. Each fragment was transferred directly to the resin 1-inch round mold; using a syringe, 1.5 mL of resin was measured and injected into the mold. The resin was Solarez UV resin (Wahoo International). The mold was placed at the center of a metal plate, which was 8 cm away from the UV source (SI Appendix, Fig. S4 and Movie S1). The UV light source (Jaxman U1c Flood flashlight) emitted light at wavelength 365 nm. A transparent box contained the UV light, a remotely controlled circuit (433 MHz Wireless RF Remote Control Switch Transmitter Receiver) powered by a remote controller (BWSS DC 12V 2CH RF Remote Relay Switch) and two 12V batteries (RS Pro-2000 mAh NiMH AA Rechargeable Battery, 12V) to power the UV light and the remote-control circuit. The transparent box was sealed to the metal plate with a Viton O-ring, and the whole assembly was placed on ice with the metal plate in direct contact with ice (SI Appendix, Fig. S4). The box was evacuated by pumping down with a rotary pump three times, 5 min each and venting after each evacuation to remove any air bubbles, make ethanol evaporate, and suck Solarez resin into as many coral pores as possible. Then the valve was closed and the sample left in static vacuum.

The UV flashlight was switched on using the remote control and left on for 15 min to cure the Solarez resin. The box was vented to check if the resin was fully cured. If the sample was not yet hard, it was removed from the mold, flipped upside-down, and exposed to UV for an additional 10 min.

Using Solarez resin and UV curing allowed us to substantially shorten the time between death of the animal and analysis. The ice kept the temperature low during curing, which is essential for this experiment, because the heat released by exothermic resin curing is sufficient to make ACC crystallize. The vacuum was necessary for better infiltrating the coral sample, and for preventing condensation of atmospheric moisture on the sample, because contact with water also makes ACC crystallize (58).

After UV-curing, each sample was polished, coated with 1-nm Pt in the area of interest and 40-nm Pt around it, as described previously (33, 72, 73), imaged with PLM, and inserted into ultrahigh vacuum for PEEM analysis.

The *S. pistillata* sample for SI Appendix, Fig. S2 was embedded in EpoFix (EMS), before polishing and imaging at the PLM.

PEEM

In all PEEM experiments in this work, the lateral resolution was 60 nm and the probing depth 3 nm. PEEM experiments were done at the Advanced Light Source on beamline 11.0.1.1 at the Ca L-edge for component mapping and [Ca] mapping, and at the O K-edge for PIC mapping of all samples. These methods were described previously (33, 38, 39). We limited the magnification and resolution to shorten the acquisition time and therefore reduce the radiation dose on the samples. This limits radiation damage (74) and most importantly maintains the amorphous phases amorphous. Extensive exposure makes the amorphous phases crystallize (38).

Briefly, for component maps stacks of PEEM images with 60-nm pixels and 60-μm field-of-view were acquired while scanning the illuminating X-ray photon energy across the Ca L-edge, from 340 to 360 eV, with 0.1-eV energy steps between 345 and 355 eV and 0.5 eV from 340 to 345 eV and 355 to 360 eV.

All Ca data were taken with circular polarization to avoid any linear polarization effects from crystals. The 121 images were converted to 8-bit tif stacks using Igor Pro Carbon and the GG Macros developed for component analysis by our group, and available to any interested users free of charge (https://home.physics.wisc.edu/gilbert/software/). A new set of component spectra termed CY1 was extracted from the present data, averaging 100 to 900 single-pixel spectra from multiple stacks to avoid nonstatistical noise, aligned, averaged, and peak-fitted to produce noise-free component spectra. The new CY1 components ACC-H_2O, ACC, and aragonite are presented in SI Appendix, Fig. S1 and are consistent with all previously published spectra (33, 36–39, 75).

Each pixel of each stack contained a Ca L-edge spectrum of an unknown mineral phase. This spectrum was best-fitted (https://home.physics.wisc.edu/gilbert/software/) with a linear combination of the three component spectra, and the proportion of each component was then displayed as an RGB color. After >30 h postmortem no ACC-H_2O or ACC were detected in any pixels. All component maps presented here were acquired between 14 and 30 h postmortem.

For all corals we compared component maps obtained using the “0823” component spectra used in Mass et al. (33), with those obtained using the newly extracted “CY1” component spectra, with consistent results. The main difference is that 0823 components found more amorphous pixels, but they also found some undesirable displaced amorphous nanoparticles nestled into polishing scratches. CY1 found fewer amorphous pixels, but never scratches, thus CY1 are less sensitive to both amorphous phases and artifacts; they are, therefore, more conservative component spectra, and this is why they were selected for all data presented here.

For PIC maps (76–78), once all of the time-sensitive Ca stacks were acquired in each sample, stacks of PEEM images with 60-nm pixels and 60-μm field of view were acquired with constant illuminating X-ray photon energy at 534 eV, the energy position of the oxygen K-edge Π* peak, which is most sensitive to polarization and crystal orientation. The stacks were acquired while scanning the linear polarization direction in the illuminating monochromatic X-rays, from horizontal to vertical in 5° steps. The resulting 19 images were converted and mounted as a stack, then processed to measure the crystal *c*-axis orientation in 3D and display it quantitatively in a PIC map. The in-plane (hue) and off-plane (brightness) polar coordinates are displayed as color, according to the color bars in Figs. 3*A2* and 4 *C* and *F*. Both in-plane and off-plane angles are measured with respect to the polarization plane, which forms a 60° angle with the image plane, since the vertically mounted sample surface is illuminated from the right, at 30° grazing incidence (21, 79).

PLM of Coral Samples

All coral samples embedded, polished, and coated were imaged with crossed polarizers before PEEM analysis, so the PLM images could be used to navigate on the sample during the PEEM experiment, and to record where, precisely, each set of PEEM data were acquired. All PLM images were acquired using either a Nikon MM-40 Measuring Microscope (Figs. 2*A* and 3 *A1–G1* and SI Appendix, Fig. S2) or a Nikon MM-400 Measuring Microscope (SI Appendix, Fig. S2) at the Advanced Light Source. Both microscopes work in reflected light, illuminate the sample from the top with fixed linear polarization (illumination channel) and detect reflected light with rotatable polarization (analysis channel). Reflected-light microscopes are ideal to observe the top surface of a polished sample, which is what PEEM analyzes. Images were acquired using 5×, 20×, and 50× objectives, and ~10× on the eyepiece or camera port. In Fig. 2, the objectives used were 20× (Fig. 2 *A*) or a 5× (Fig. 2 *B*). The angle between the two polarization channels was ~90°, varying between 85° and 110°, wherever the contrast between crystal orientations appeared maximum in each sample. In addition, the PLM images revealed bright colorful growth fronts in many of the samples, which are interpreted as due to form birefringence of micro- or nanoporous regions of the skeleton, as observed in other systems (45–47).

Supplementary Material

Refer to Web version on PubMed Central for supplementary material.

Acknowledgments

We thank Guy Oei and Solomon Wong at the Albany Aquarium for maintaining aquaria and all living corals used here; Wenming Dong and Carl Steefel for the Brunauer-Emmett-Teller experiments at Lawrence Berkeley National Laboratory; Richard Celestre, Jun Zhang, and Drue Hood-McFadden for sample preparations; and Alexander Venn for discussions. P.U.P.A.G. acknowledges 80% support from the US Department of Energy, Office of Science, Office of Basic Energy Sciences, Chemical Sciences, Geosciences, and Biosciences Division, under Award DE-FG02-07ER15899, and 20% support from National Science Foundation Grant DMR-1603192. T.M. acknowledges that this project has received funding from the European Research Council under the European Union's Horizon 2020 research and innovation programme (Grant 755876). The PhotoEmission Electron Microscopy experiments were done at the Advanced Light Source, which is supported by the Director, Office of Science, Office of Basic Energy Sciences, US Department of Energy under Contract DE-AC02-05CH11231.

Data Availability

All study data are included in the article and supporting information. Code and materials used in the analysis are available to any researcher to reproduce or extend the analysis in Zenodo (https://doi.org/10.5281/zenodo.4245677).

References

1. Hoegh-Guldberg O, et al. Coral reefs under rapid climate change and ocean acidification. Science. 2007; 318:1737–1742. [PubMed: 18079392]
2. Pandolfi JM, Connolly SR, Marshall DJ, Cohen AL. Projecting coral reef futures under global warming and ocean acidification. Science. 2011; 333:418–422. [PubMed: 21778392]
3. Hughes TP, et al. Global warming and recurrent mass bleaching of corals. Nature. 2017; 543:373–377. [PubMed: 28300113]

4. Scheufen T, Krämer WE, Iglesias-Prieto R, Enríquez S. Seasonal variation modulates coral sensibility to heat-stress and explains annual changes in coral productivity. Sci Rep. 2017; 7:1–15. [PubMed: 28127051]
5. Carpenter KE, et al. One-third of reef-building corals face elevated extinction risk from climate change and local impacts. Science. 2008; 321:560–563. [PubMed: 18653892]
6. Eyre BD, et al. Coral reefs will transition to net dissolving before end of century. Science. 2018; 359:908–911. [PubMed: 29472482]
7. Wild C, et al. Climate change impedes scleractinian corals as primary reef ecosystem engineers. Mar Freshw Res. 2011; 62:205–215.
8. Muscatine L, et al. Stable isotopes (δ13C and δ15N) of organic matrix from coral skeleton. Proc Natl Acad Sci U S A. 2005; 102:1525–1530. [PubMed: 15671164]
9. Cohen AL, McConnaughey TA. Geochemical perspectives on coral mineralization. Rev Mineral Geochem. 2003; 54:151–187.
10. Falkowski PG, Dubinsky Z, Muscatine L, Porter JW. Light and the bioenergetics of a symbiotic coral. Biosci. 1984; 34:705–709.
11. Eder M, Amini S, Fratzl P. Biological composites—Complex structures for functional diversity. Science. 2018; 362:543–547. [PubMed: 30385570]
12. Constantz B, Weiner S. Acidic macromolecules associated with the mineral phase of scleractinian coral skeletons. J Exp Zool. 1988; 248:253–258.
13. Cuif JP, Dauphin Y, Berthet P, Jegoudez J. Associated water and organic compounds in coral skeletons: Quantitative thermogravimetry coupled to infrared absorption spectrometry. Geochem Geophys Geosys. 2004; doi: 10.1029/2004GC000783
14. Tambutté S, et al. Coral biomineralization: From the gene to the environment. J Exp Mar Biol Ecol. 2011; 408:58–78.
15. Drake JL, et al. How corals made rocks through the ages. Glob Change Biol. 2020; 26:31–53.
16. Falini G, Fermani S, Goffredo S. Coral biomineralization: A focus on intra-skeletal organic matrix and calcification. Semin Cell Develop Biol. 2015; 46:17–26.
17. Stolarski J. Three-dimensional micro-and nanostructural characteristics of the scleractinian coral skeleton: A biocalcification proxy. Acta Palaeontol Pol. 2003; 48
18. Coronado I, Fine M, Bosellini FR, Stolarski J. Impact of ocean acidification on crystallographic vital effect of the coral skeleton. Nat Commun. 2019; 10:1–9. [PubMed: 30602773]
19. Cuif J-P, Dauphin Y. Microstructural and physico-chemical characterization of ‘centers of calcification’in septa of some Recent scleractinian corals. Palaontol Z. 1998; 72:257–269.
20. Von Euw S, et al. Biological control of aragonite formation in stony corals. Science. 2017; 356:933–938. [PubMed: 28572387]
21. Sun C-Y, et al. Spherulitic growth of coral skeletons and synthetic aragonite: Nature’s three-dimensional printing. ACS Nano. 2017; 11:6612–6622. [PubMed: 28564539]
22. Sun C-Y, et al. Crystal nucleation and growth of spherulites demonstrated by coral skeletons and phase-field simulations. Acta Biomater. 2020; doi: 10.1016/j.actbio.2020.06.027
23. De Yoreo JJ, et al. Crystallization by particle attachment in synthetic, biogenic, and geologic environments. Science. 2015; 349:aaa6760. [PubMed: 26228157]
24. Venn A, Bernardet C, Chabenat A, Tambutté E, Tambutté S. Paracellular transport to the coral calcifying medium: Effects of environmental parameters. J Exp Biol. 2020; 223:jeb227074. [PubMed: 32675232]
25. Ganot P, et al. Ubiquitous macropinocytosis in anthozoans. eLife. 2020; 9:e50022. [PubMed: 32039759]
26. Sevilgen DS, et al. Full in vivo characterization of carbonate chemistry at the site of calcification in corals. Sci Adv. 2019; 5:eaau7447. [PubMed: 30746460]
27. Gilbert PU, et al. Biomineralization by particle attachment in early animals. Proc Natl Acad Sci U S A. 2019; 116:17659–17665. [PubMed: 31427519]
28. Wall M, et al. Linking internal carbonate chemistry regulation and calcification in corals growing at a Mediterranean CO2 vent. Front Mar Sci. 2019; doi: 10.3389/fmars.2019.00699

29. National Academies of Sciences. A Research Review of Interventions to Increase the Persistence and Resilience of Coral Reefs. National Academies of Sciences; 2019.
30. National Academies of Sciences. A Decision Framework for Interventions to Increase the Persistence and Resilience of Coral Reefs. National Academies of Sciences; 2019.
31. Constantz BR. Coral skeleton construction: A physiochemically dominated process. Palaios. 1986; 1:152–157.
32. Holcomb M, et al. Coral calcifying fluid pH dictates response to ocean acidification. Sci Rep. 2014; 4:5207. [PubMed: 24903088]
33. Mass T, et al. Amorphous calcium carbonate particles form coral skeletons. Proc Natl Acad Sci U S A. 2017; 114:E7670–E7678. [PubMed: 28847944]
34. Beniash E, Aizenberg J, Addadi L, Weiner S. Amorphous calcium carbonate transforms into calcite during sea urchin larval spicule growth. Proc R Soc B Biol Sci. 1997; 264:461–465.
35. Politi Y, Arad T, Klein E, Weiner S, Addadi L. Sea urchin spine calcite forms via a transient amorphous calcium carbonate phase. Science. 2004; 306:1161–1164. [PubMed: 15539597]
36. Politi Y, et al. Transformation mechanism of amorphous calcium carbonate into calcite in the sea urchin larval spicule. Proc Natl Acad Sci U S A. 2008; 105:17362–17366. [PubMed: 18987314]
37. Killian CE, et al. The mechanism of calcite co-orientation in the sea urchin tooth. J Am Chem Soc. 2009; 131:18404–18409. [PubMed: 19954232]
38. Gong YUT, et al. Phase transitions in biogenic amorphous calcium carbonate. Proc Natl Acad Sci U S A. 2012; 109:6088–6093. [PubMed: 22492931]
39. DeVol RT, et al. Nanoscale transforming mineral phases in fresh nacre. J Am Chem Soc. 2015; 137:13325–13333. [PubMed: 26403582]
40. Winter MR, Morgulis M, Gildor T, Cohen AR, de-Leon SB-T. Calcium-vesicles perform active diffusion in the sea urchin embryo during larval biomineralization. bioRxiv. 2020 Aug 15.doi: 10.1101/2020.08.14.244053
41. Stapane L, et al. Avian eggshell formation reveals a new paradigm for vertebrate mineralization via vesicular amorphous calcium carbonate. J Biol Chem. 2020; doi: 10.1074/jbc.RA120.014542
42. Venn A, Tambutté E, Holcomb M, Allemand D, Tambutté S. Live tissue imaging shows reef corals elevate pH under their calcifying tissue relative to seawater. PLoS One. 2011; 6:e20013. [PubMed: 21637757]
43. Gower LB, Odom DJ. Deposition of calcium carbonate films by a polymer-induced liquid-precursor (PILP) process. J Cryst Growth. 2000; 210:719–734.
44. Wallace AF, et al. Microscopic evidence for liquid-liquid separation in supersaturated CaCO3 solutions. Science. 2013; 341:885–889. [PubMed: 23970697]
45. Oldenbourg R, Salmon E, Tran P. Birefringence of single and bundled microtubules. Biophys J. 1998; 74:645–654. [PubMed: 9449366]
46. Rädler JO, Koltover I, Salditt T, Safinya CR. Structure of DNA-cationic liposome complexes: DNA intercalation in multilamellar membranes in distinct interhelical packing regimes. Science. 1997; 275:810–814. [PubMed: 9012343]
47. Prusiner SB, et al. Scrapie prions aggregate to form amyloid-like birefringent rods. Cell. 1983; 35:349–358. [PubMed: 6418385]
48. Yang L, Killian CE, Kunz M, Tamura N, Gilbert PUPA. Biomineral nanoparticles are space-filling. RSC-Nanoscale. 2011; 3:603–609.
49. McHale J, Auroux A, Perrotta A, Navrotsky A. Surface energies and thermodynamic phase stability in nanocrystalline aluminas. Science. 1997; 277:788–791.
50. Rosenfeld M, Yam R, Shemesh A, Loya Y. Implication of water depth on stable isotope composition and skeletal density banding patterns in a Porites lutea colony: Results from a long-term translocation experiment. Coral Reefs. 2003; 22:337–345.
51. Gladfelter EH, Monahan RK, Gladfelter WB. Growth rates of five reef-building corals in the northeastern Caribbean. Bull Mar Sci. 1978; 28:728–734.
52. Neder M, et al. Mineral formation in the primary polyps of pocilloporoid corals. Acta Biomater. 2019; 96:631–645. [PubMed: 31302296]

53. Croize D, Renard F, Gratier J-P. Compaction and porosity reduction in carbonates: A review of observations, theory, and experiments. Adv Geophys. 2013; 54:181–238.
54. Mucci A. The solubility of calcite and aragonite in seawater at various salinities, temperatures, and one atmosphere total pressure. Am J Sci. 1983; 283:780–799.
55. Olszta M, Douglas E, Gower L. Scanning electron microscopic analysis of the mineralization of type I collagen via a polymer-induced liquid-precursor (PILP) process. Calcif Tissue Int. 2003; 72:583–591. [PubMed: 12616327]
56. Schenk AS, et al. Polymer-induced liquid precursor (PILP) phases of calcium carbonate formed in the presence of synthetic acidic polypeptides—Relevance to bio-mineralization. Faraday Discuss. 2012; 159:327–344.
57. Comeau S, Cornwall C, McCulloch M. Decoupling between the response of coral calcifying fluid pH and calcification to ocean acidification. Sci Rep. 2017; 7:1–10. [PubMed: 28127051]
58. Radha AV, Forbes TZ, Killian CE, Gilbert PUPA, Navrotsky A. Transformation and crystallization energetics of synthetic and biogenic amorphous calcium carbonate. Proc Natl Acad Sci U S A. 2010; 107:16438–16443. [PubMed: 20810918]
59. Gal A, et al. Particle accretion mechanism underlies biological crystal growth from an amorphous precursor phase. Adv Funct Mater. 2014; 24:5420–5426.
60. Gagnon AC, Adkins JF, Erez J. Seawater transport during coral biomineralization. Earth Planet Sci Lett. 2012; 329:150–161.
61. Tambutté S, et al. Characterization and role of carbonic anhydrase in the calcification process of the azooxanthellate coral Tubastrea aurea. Mar Biol. 2007; 151:71–83.
62. Orrenius S, McConkey DJ, Bellomo G, Nicotera P. Role of Ca2+ in toxic cell killing. Trends Pharmacol Sci. 1989; 10:281–285. [PubMed: 2672472]
63. Holcomb M, Cohen AL, Gabitov RI, Hutter JL. Compositional and morphological features of aragonite precipitated experimentally from seawater and biogenically by corals. Geochim Cosmochim Acta. 2009; 73:4166–4179.
64. Tambutté E, et al. Calcein labelling and electrophysiology: insights on coral tissue permeability and calcification. Proc R Soc Biol Sci. 2012; 279:19–27.
65. Ganot P, et al. Structural molecular components of septate junctions in cnidarians point to the origin of epithelial junctions in eukaryotes. Mol Biol Evol. 2015; 32:44–62. [PubMed: 25246700]
66. Erez J. The source of ions for biomineralization in foraminifera and their implications for paleoceanographic proxies. Rev Mineral Geochem. 2003; 54:115–149.
67. Blue CR, et al. Chemical and physical controls on the transformation of amorphous calcium carbonate into crystalline CaCO3 polymorphs. Geochim Cosmochim Acta. 2017; 196:179–196.
68. Erez J. Vital effect on stable-isotope composition seen in foraminifera and coral skeletons. Nature. 1978; 273:199–202.
69. Dunbar RB, Wellington GM. Stable isotopes in a branching coral monitor seasonal temperature variation. Nature. 1981; 293:453–455.
70. Weber JN, Woodhead PM. Temperature dependence of oxygen-18 concentration in reef coral carbonates. J Geophys Res. 1972; 77:463–473.
71. Erez, J, Reynaud, S, Silverman, J, Schneider, K, Allemand, D. Coral calcification under ocean acidification and global changeCoral Reefs: An Ecosystem in Transition. Dubinsky, Z, Stambler, N, editors. Springer; 2011. 151–176.
72. De Stasio G, Frazer BH, Gilbert B, Richter KL, Valley JW. Compensation of charging in X-PEEM: A successful test on mineral inclusions in 4.4 Ga old zircon. Ultramicroscopy. 2003; 98:57–62. [PubMed: 14609643]
73. Gilbert, PUPA. Photoemission spectromicroscopy for the biomineralogistBiomineralization Sourcebook, Characterization of Biominerals and Biomimetic Materials. DiMasi, E, Gower, LB, editors. CRC Press; Boca Raton, FL: 2014. 135–151.
74. Parasassi T, Sapora O, Giusti AM, De Stasio G, Ravagnan G. Alterations in erythrocyte-membrane lipids induced by low-doses of ionizing-radiation as revealed by 1,6-diphenyl-1,3,5-hexatriene fluorescence lifetime. Int J Radiat Biol. 1991; 59:59–69. [PubMed: 1671076]

75. Albéric M, et al. Growth and regrowth of adult sea urchin spines involve hydrated and anhydrous amorphous calcium carbonate precursors. J Struct Biol X. 2019; 1:1000004.

76. DeVol RT, et al. Oxygen spectroscopy and polarization-dependent imaging contrast (PIC)-mapping of calcium carbonate minerals and biominerals. J Phys Chem B. 2014; 118:8449–8457. [PubMed: 24821199]

77. Olson IC, et al. Crystal lattice tilting in prismatic calcite. J Struct Biol. 2013; 183:180–190. [PubMed: 23806677]

78. Metzler RA, et al. Polarization-dependent imaging contrast in abalone shells. Phys Rev B. 2008; 77:064110.

79. Gilbert PUPA, Young A, Coppersmith SN. Measurement of c-axis angular orientation in calcite (CaCO3) nanocrystals using X-ray absorption spectroscopy. Proc Natl Acad Sci U S A. 2011; 108:11350–11355. [PubMed: 21693647]

Europe PMC Funders Author Manuscripts

Europe PMC Funders Author Manuscripts

Significance

Whether reef-building corals form their skeletons ion by ion from solution or by amorphous particle attachment has important implications for isotope incorporation and for understanding coral skeletons' resilience to ocean warming and acidification. Here we show that all kinds of reef-building corals make their skeletons by attachment of amorphous nanoparticles and fill the spaces between nanoparticles ion by ion. Thus, the dual mechanism of ionand particle- attachment is general and relevant to reef formation, which provides the infrastructure for one of the most diverse ecosystems on Earth.

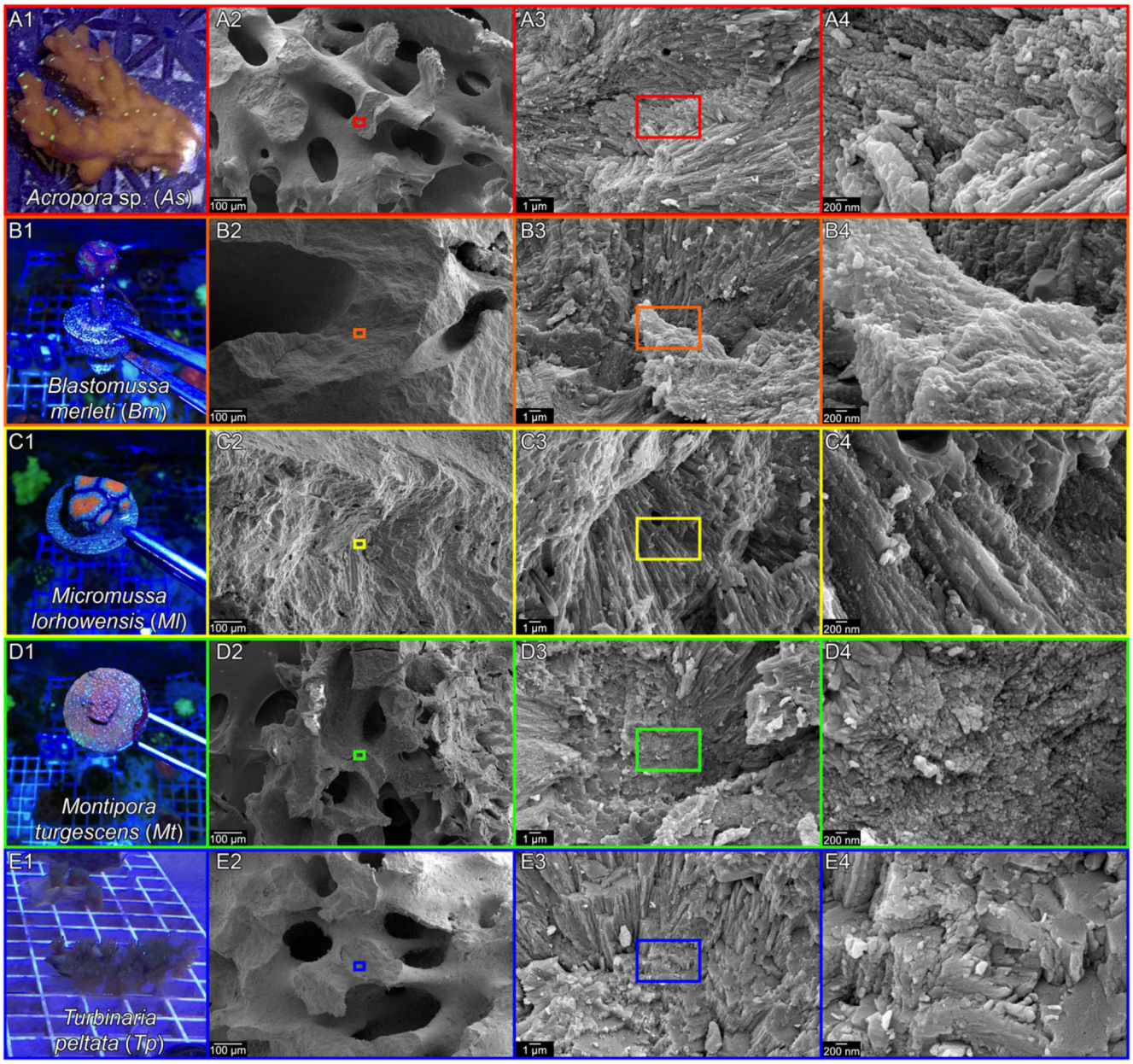

Fig. 1.

Photographs and SEM images of the five new coral species analyzed here. The photographs in *A1–E1* show living corals still in the aquarium. For each coral, the genus, species, and their abbreviations are in *A1–E1*. The SEM images were acquired on fractured surfaces to show the nanoparticulate nature of all skeletons. Boxes in *A2–E2* and *A3–E3* indicate the position where the images in *A3–E3* and *A4–E4* were acquired. All species display 50 to 400 nm nanoparticles (*A4–E4*).

Europe PMC Funders Author Manuscripts

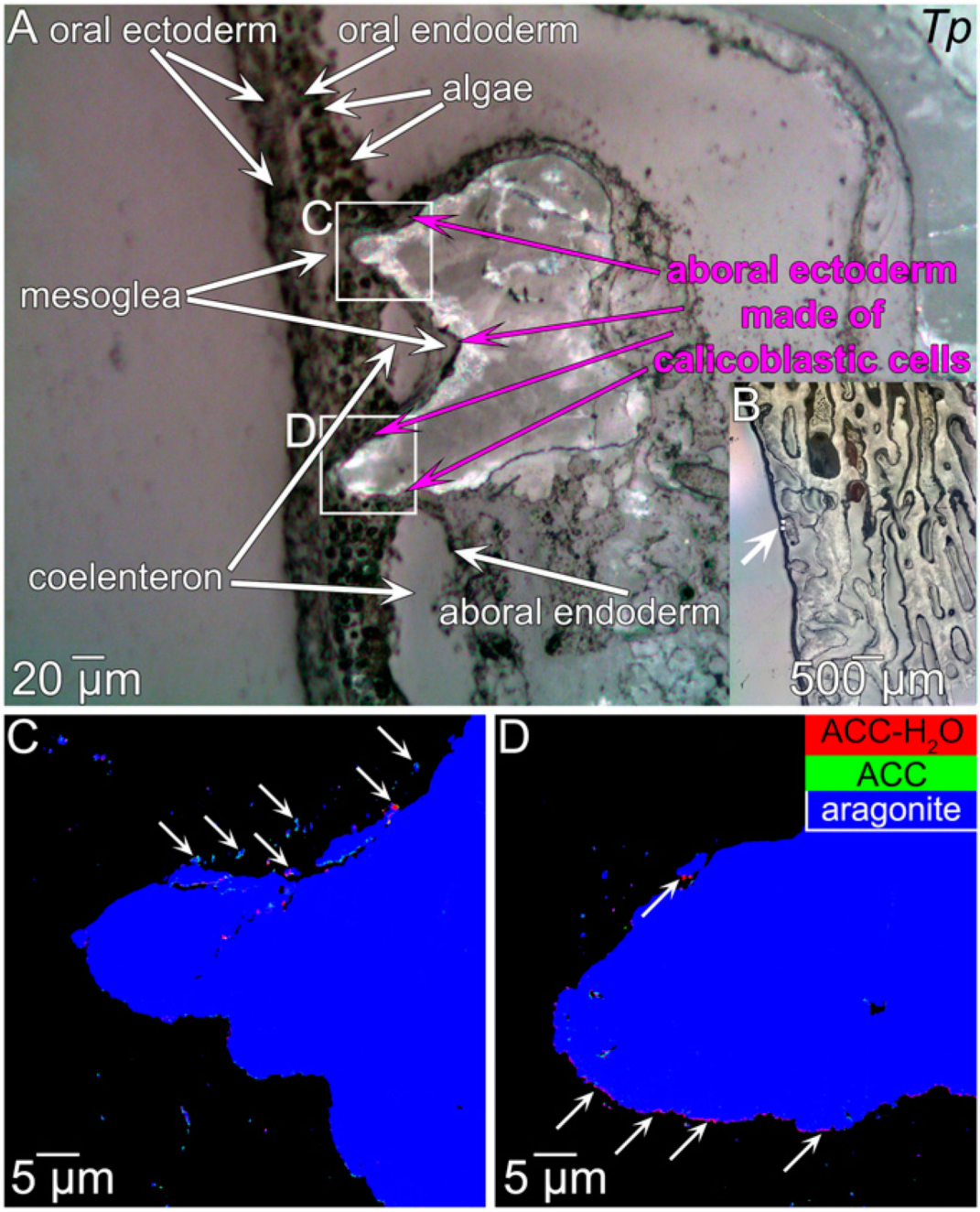

Fig. 2.

Tissues, mature, and forming skeleton from *T. peltata* (*Tp*). (*A* and *B*) PLM images. The boxes in a indicate were the data in *C* and *D* were acquired. The micrograph in *A* is labeled with all relevant and recognizable tissue components. Starting from the outside (seawater side of the polyp), there are four layers of distinct tissues: Oral ectoderm and oral endoderm, which are separated by a layer of mesoglea, aboral endoderm and aboral ectoderm, separated by another layer of mesoglea. The coelenteron is the space separating the oral from the aboral layers. The fourth tissue in direct or close contact with the growing skeleton is the

aboral ectoderm, or calicoderm because it is made of calicoblastic cells, which closely envelope the skeleton (magenta arrows). The arrow in *B* points to the two areas in *C* and *D*. (*C* and *D*) Component maps, obtained by PEEM at the Ca L-edge, in which the mineral phases in each pixel are represented by color, according to the legend in *D*. Notice in *C* and *D* the nanoparticles outside the skeleton, which are clearly in the tissue region, especially at the top of *C* (arrows). A layer of red (ACC-H_2O) nanoparticles lines the bottom of the skeleton in *D* (arrows). In *A*, the band at the growth front of the skeleton is interpreted to be bright and colorful in PLM due to birefringence of nano- or microsize anisotropic particles in the porous aggregate.

Europe PMC Funders Author Manuscripts

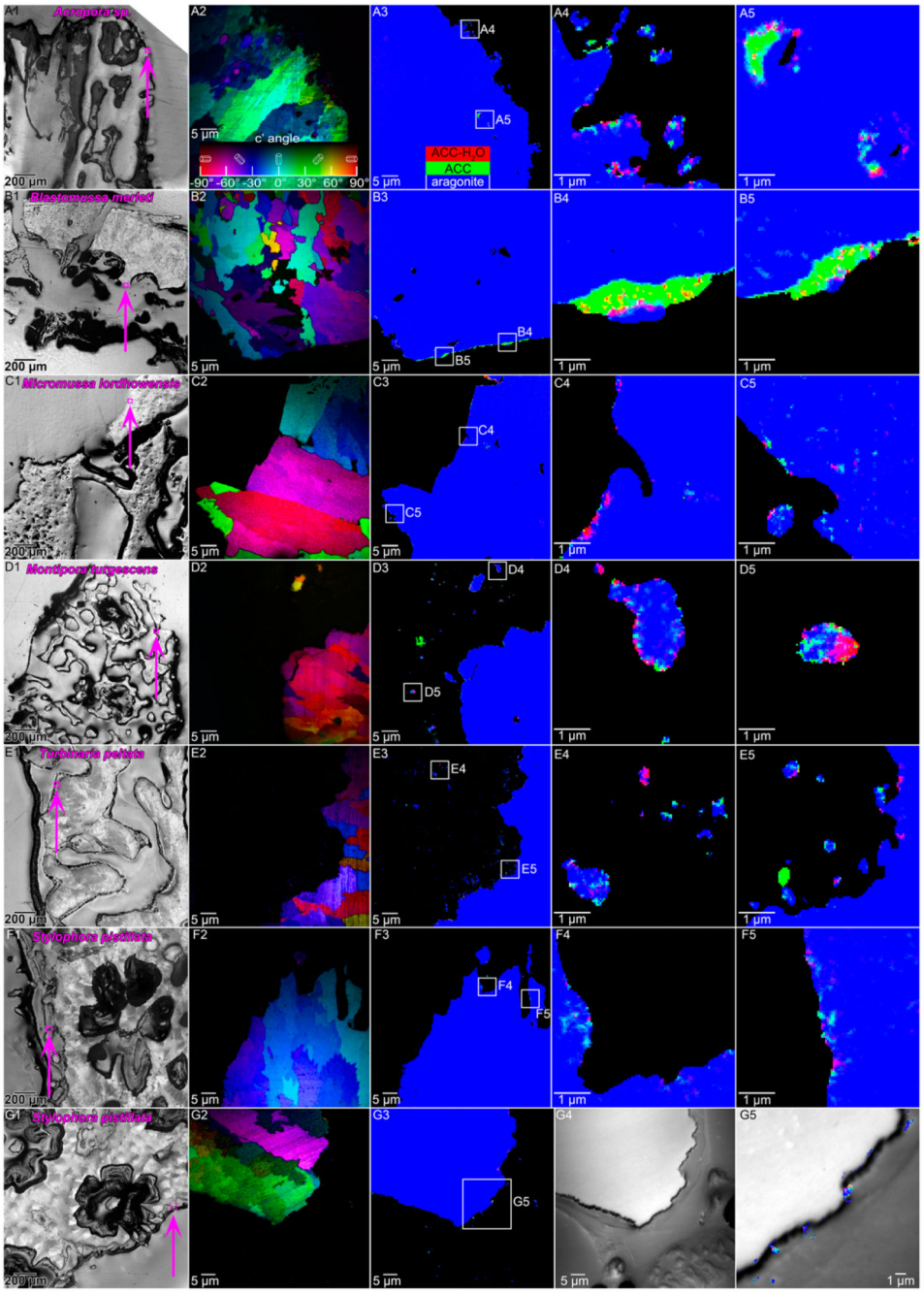

Fig. 3.

Amorphous precursors in the six coral species in Table 1. (*A1–G1*) PLM image of each polished sample where the area in *A2–G2* and *A3–G3* is indicated by a magenta box and arrow. (*A2–G2*) PIC map where color indicates crystal orientation according to the color legend in *A2*. (*A3–G3*) PEEM component map where color indicates mineral phases in each 60-nm pixel, according to the color legend in *A3*. (*A4–F4* and *A5–F5*) Details from white boxes in *A3–F3*, magnifying the few still amorphous pixels. (*G*) Amorphous precursor particles in tissue. (*G4*) PEEM image including the skeleton growth front and tissue

components as labeled in SI Appendix, Fig. S5. (*G5*) Overlaid image and map from *G3* and *G4* of the calicoblastic cell layer enveloping the growth front of the skeleton. Mature skeleton aragonite and epoxy were removed for clarity. Notice all three phases in intracellular Ca-rich particles.

Europe PMC Funders Author Manuscripts

Europe PMC Funders Author Manuscripts

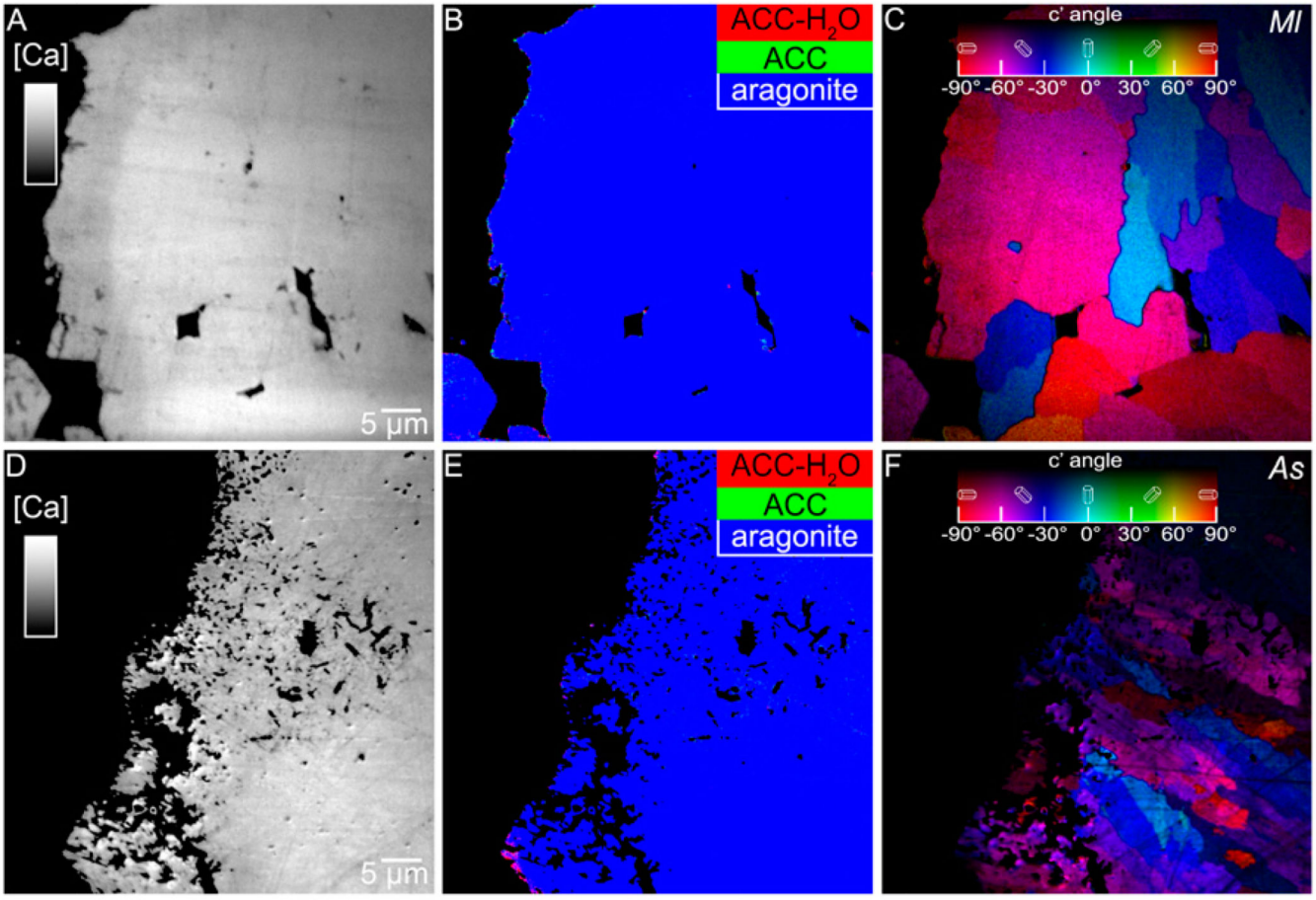

Fig. 4.

Comparison of [Ca] maps, component maps, and PIC maps of the same area at the growth surfaces of fresh, forming skeletons of *M. lordhowensis* (*Ml*) (*A*–*C*) and *Acropora* sp. (*As*) (*D*–*F*). (*A*) Notice the 7- to 8-µm-thick low-[Ca] band at the forming surface in a (left edge). As indicated by the grayscale bar, brightness is proportional to [Ca], but is not calibrated. Resin with no Ca is black, crystalline aragonite is bright gray in mature skeleton (right side). (*D*) [Ca] map showing the 15-µm-wide microporous band at the forming surface (left). In *D* the [Ca] is identical in the microporous and the space-filled regions (left and right, respectively), indicating that each particle on the left is fully dense, but particles do not fill space, they are interspersed with the embedding resin. (*B* and *E*) Component maps showing a few amorphous pixels at the growing surfaces. The low-[Ca] band in a is mostly crystalline aragonite (blue pixels) in the component map in *B*. Also, in *E*, most pixels are evenly crystalline aragonite (blue), in both the microporous layer and the bulk mature skeleton. (*C* and *F*) PIC map, where the orientation of the aragonite crystal in each 60-nm pixel is measured and quantitatively displayed in color, including hue and brightness, corresponding to in-plane and off-plane angles in polar coordinates.

Europe PMC Funders Author Manuscripts

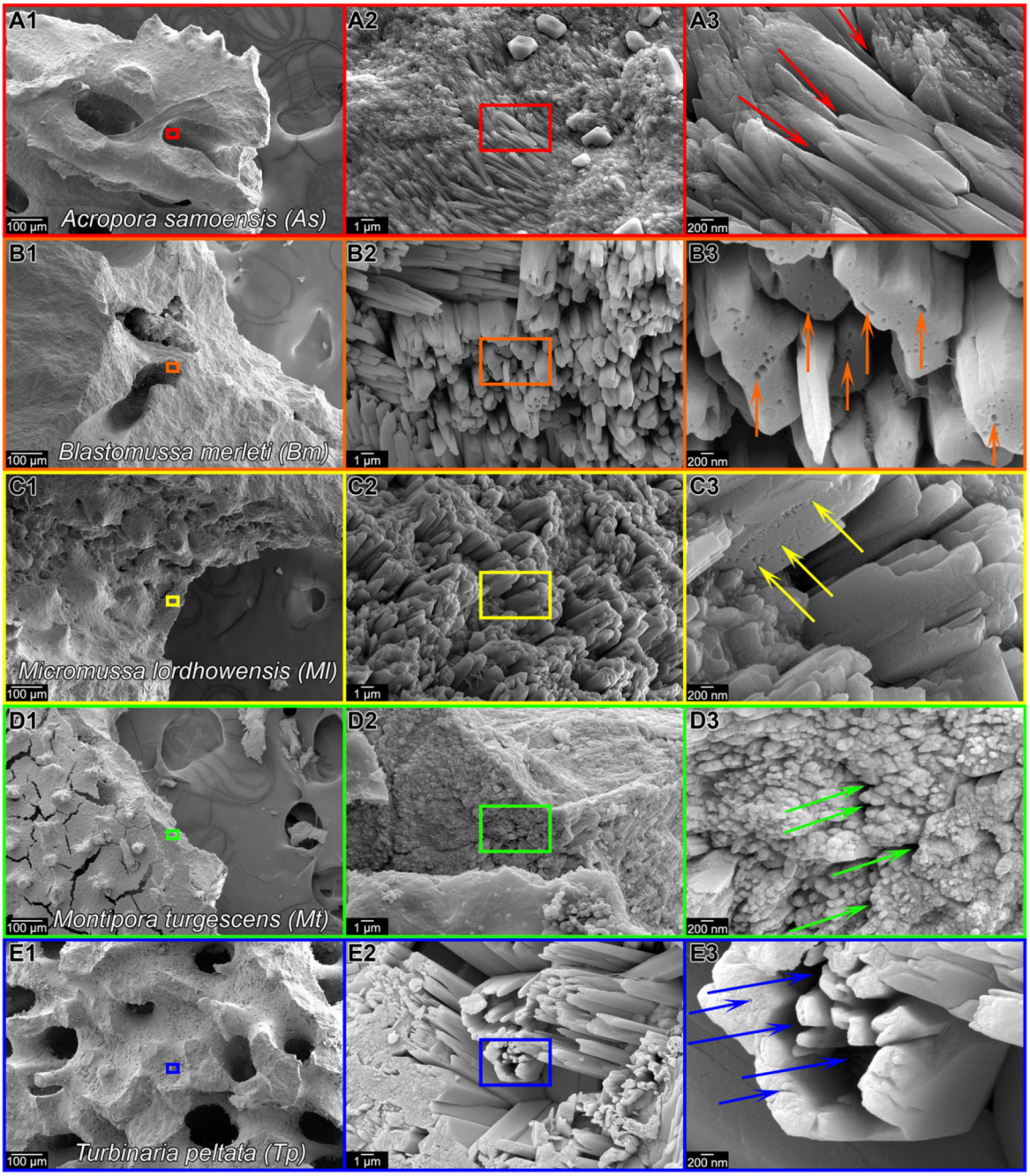

Fig. 5.

SEM images of the native surface of forming coral skeletons. Increasing magnifications reveal micro- and nanoscale porosity of surfaces as indicated by arrows at the high-magnification images in *A3–E3*. In *D1* and *D2* the dried and cracked tissue is visible (bottom left) but the magnified region is on the skeleton surface (*D3*).

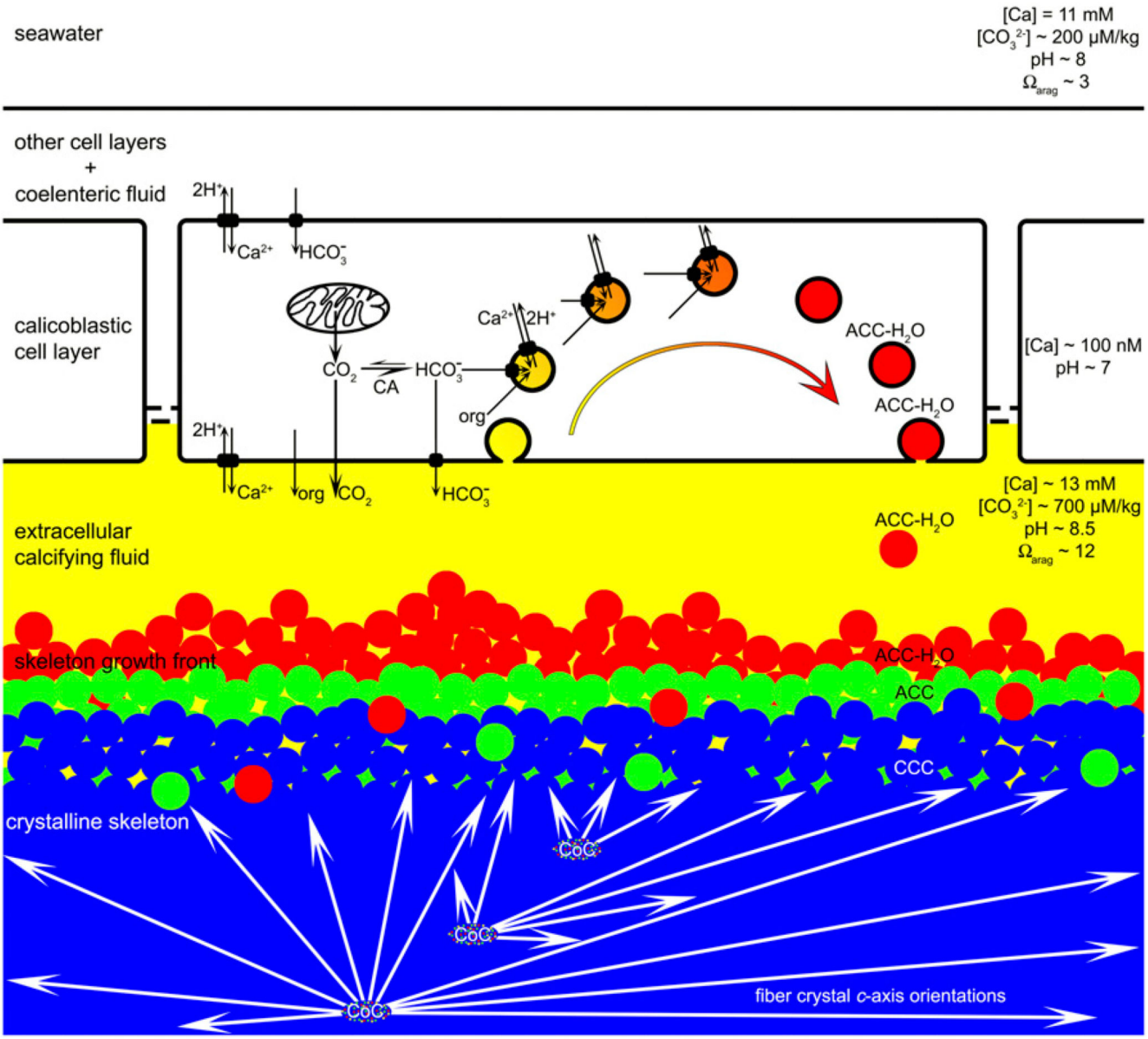

Fig. 6.

Model of coral skeleton formation combining nanoparticles and ion-by-ion growth. The values for calcium and carbonate concentrations ([Ca], [CO_3^{2-}]), pH, and supersaturation with respect to aragonite (Ω_{arag}) in calcifying fluid and seawater were measured by Sevilgen et al. (26). The CF is endocytosed into a calicoblastic cell from its apical side (bottom) by macropinocytosis (25), enriched in Ca, HCO_3^-, other ions, organics; protons are removed, so ACC-H_2O nanoparticles can form (red). These are then exocytosed into the CF and attach to the growing skeleton. Gradually the solid aggregate of nanoparticles and ions dehydrates (green), crystallizes (blue), and ion attachment fills interstitial spaces. Crystalline fibers radiate from CoCs, and form spherulites (21), as each crystal fiber grows at the expense of the amorphous precursor phases. All three phases persist in CoCs.

Europe PMC Funders Author Manuscripts

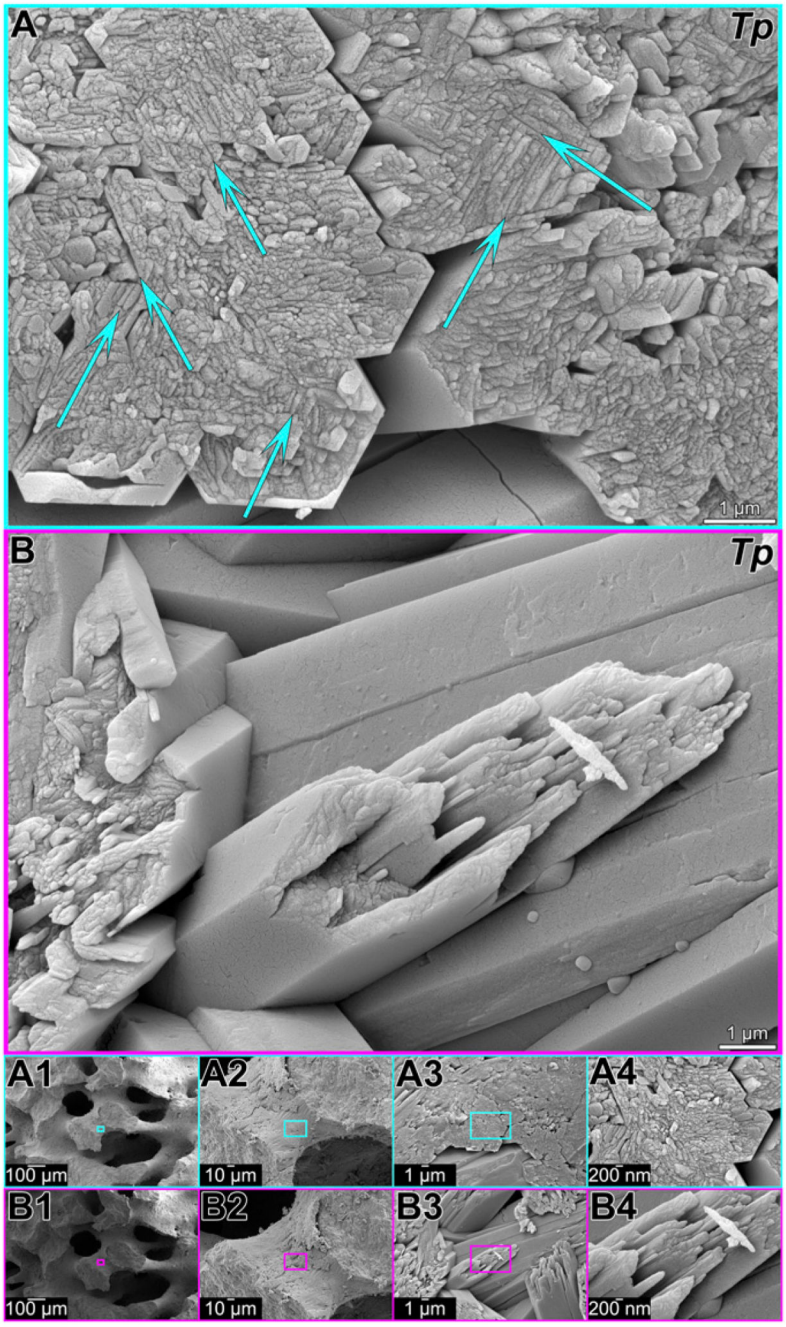

Fig. 7.

SEM images of the native surface of *T. peltata* (*Tp*) skeleton showing the dual mechanism of particle attachment and ion-by-ion filling in forming coral skeleton fibers. The outer surface of each fiber in *A* and *B* appears as a euhedral pseudohexagonal prism, with a smooth lateral surface that is space-filling; thus, it must have grown by both particle attachment and ion-by-ion filling. Interspersed with euhedral crystals are nonspace-filling nanoparticles. Increasing magnification images in *A1–A4* and *B1–B4* show where on the native surface the images in *A* and *B* were acquired. Particles may attach preferentially in euhedral pseudohexagonal

prism geometry, thus, surfaces parallel to the outer pseudohexagonal edges are recognizable, as indicated by arrows in *A*. A false-color version of *B* is presented as SI Appendix, Fig. S3 to indicate space-filling and nonspace-filling crystals, both of which have at least one nanoparticulate side.

Europe PMC Funders Author Manuscripts

Europe PMC Funders Author Manuscripts

Table 1

The coral skeletons analyzed in Fig. 3

Genus and species	Clade	Morphology
Acropora sp.	Complex	Branching
Blastomussa merleti	Robust	Massive
Micromussa lordhowensis	Robust	Massive
Montipora turgescens	Complex	Encrusting
Turbinaria peltata	Complex	Table
Stylophora pistillata	Robust	Branching

All species except for *S. pistillata* are tropical, from the Indopacific, and reef-building. *S. pistillata* is subtropical, from the Red Sea. See SI Appendix, Table S1 for additional details.

Europe PMC Funders Author Manuscripts

Table 2

Coral skeletons are space-filling

Sample	Morphology	Surface area (m^2/g)
Aragonite single crystal	Pseudohexagonal prism	0.72
Blastomussa merleti	Massive	1.01
Montipora turgescens	Encrusting	0.68
Micromussa lordhowensis	Massive	2.61
Stylophora pistillata	Branching	3.53
Al_2O_3 nanoparticles from McHale et al. (49)	Aggregate	100–300

Specific surface area of selected coral skeletons measured by BET. The error is 10% on all measurements.